ADVANCED FUNCTIONAL MATERIALS
www.afm-journal.de

Coupling of Micromagnetic and Structural Properties Across the Martensite and Curie Temperatures in Miniaturized Ni-Mn-Ga Ferromagnetic Shape Memory Alloys

*A. M. Jakob, M. Hennes, M. Müller, D. Spemann, and S. G. Mayr**

Micromagnetic structure evolution in Ni-Mn-Ga ferromagnetic shape memory thin films is investigated by means of temperature dependent magnetic force microscopy (TD-MFM). The center of interest is the magnetic properties of epitaxial Ni-Mn-Ga thin films on MgO substrates across thermally induced phase transitions. Experimental results are discussed within the framework of competing magnetic interactions arising in stressed thin ferromagnetic films. Measurements on 14M martensite specimens are supplemented by three-dimensional micromagnetic simulations. Corresponding calculated MFM micrographs are compared to experimental data. The influence of twin variant dimension and orientation on micromagnetic domain formation and wall structure is depicted from a theoretical point of view. A micromagnetic model system of partial flux closure is proposed and calculated analytically to estimate a stress induced magneto crystalline anisotropy constant in austenite Ni-Mn-Ga.

1. Introduction

Yielding the ability of large strains up to 10% by applying an external magnetic field, martensite Ni-Mn-Ga has become an attractive, so called smart material for various industrial applications.[1–3] In particular, thin films of this ferromagnetic shape memory material (FSM) yield promising future applicability in miniaturized sensor- and actuator systems and are still the focus of scientific research since mechanical and magnetic characteristics at small scales differ from those of bulk material. Besides these size effects, additional influences such as thermal and intrinsic stresses—arising due to substrate/buffer layer constraints and preparation conditions—are essential.[4,5] As will be discussed here, the appearance and evolution of a micromagnetic domain structure with considerable out-of-plane components of magnetization arising in the austenite phase is one such unexpected phenomenon. MFM investigations on martensite Ni-Mn-Ga thin films have already been performed and previous work dealt with the correlation between domain size and film thickness.[6,7] In the present study, we first focus on qualitative and quantitative comparisons of experimental and simulated MFM micrographs. The presence of micrometer-sized regions with in-plane twinning, occurring in one of the samples investigated here, affects domain characteristics and is considered in simulations. Finally, we investigate the temperature dependence of domain structure at the phase transition and in austenite thin films at elevated temperatures. An attempt to estimate the stress induced uniaxial magneto crystalline anisotropy constant is given.

A. M. Jakob, M. Hennes, M. Müller, Prof. S. G. Mayr
Leibniz Institut für Oberflächenmodifizierung e.V.,
Permoserstr. 15, 04318 Leipzig, Germany
E-mail: stefan.mayr@iom-leipzig.de
A. M. Jakob, Prof. S. G. Mayr
Translationszentrum für Regenerative Medizin
Universität Leipzig
04103 Leipzig Germany
Dr. D. Spemann
Nukleare Festkörperphysik
Fakultät für Physik und Geowissenschaften
Universität Leipzig
04103 Leipzig, Germany
Prof. S. G. Mayr
Fakultät für Physik und Geowissenschaften
Universität Leipzig
04103 Leipzig, Germany

DOI: 10.1002/adfm.201300165

2. Results and Discussion

2.1. MFM Data vs Simulations

As shown in **Figure 1**, experimentally obtained MFM micrographs of samples S1 and S2 (color maps overlaid to 3D-topography) are compared to simulated MFM data. The measured topography of S1 (Figure 1a) at room temperature reveals a periodic wave-like surface pattern which originates from the twinned 14M martensite two-variant configuration. Within variant 1 (v_1) the short (and magnetically easy) c_{14M}-axis is oriented normal to surface plane, whereas it is aligned in-plane within variant 2 (v_2). Corresponding surface roughness amounts to about $\Delta h_{RMS} \approx 1$ nm. The average width of each twin variant is 50 ± 10 nm.

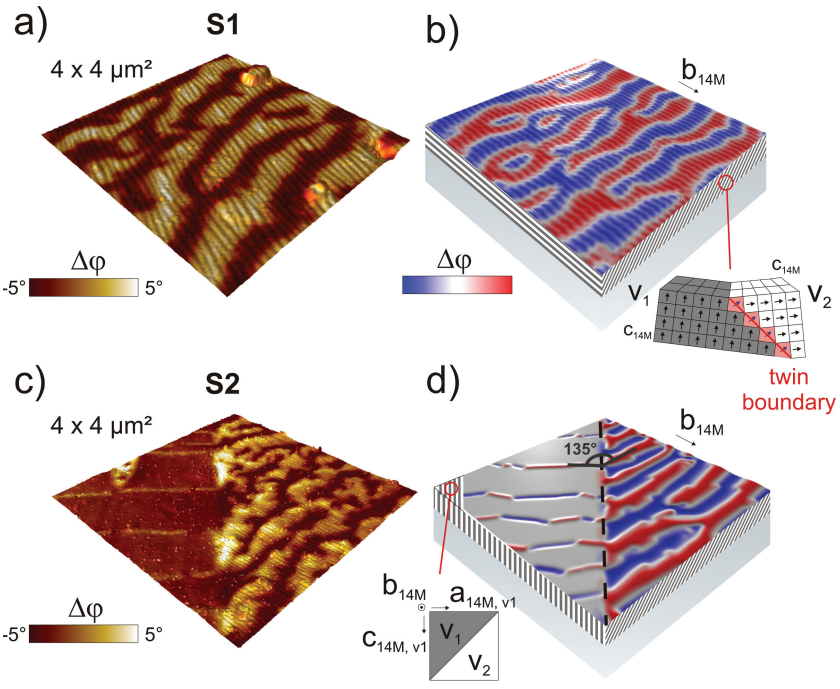

Figure 1. a,c) Experimental and b,d) theoretical results of local magnetic structures for S1 and S2. Simulations consider local magneto crystalline features, twinning periodicity as well as film thickness and MFM conditions such as tip dimensions and lift height. Schematics illustrate the presence of twin variants v_1 and v_2 as well as local orientation of the 14M modulated lattice.

MFM phase contrast exhibits a slightly disturbed but aligned magnetic domain stripe pattern crossing the twin pattern predominantly perpendicular. The out-of-plane magnetization within bright domain stripes is oriented parallel with respect to the tip magnetization (attractive force) and antiparallel in case of dark domains (repulsive). It should be noted that convention of MFM phase color contrast depends on the AFM software. The convention utilized here is the physically correct one, since increasing repulsive forces cause a frequency shift to higher values and thus a drop in phase. In general, MFM micrographs of martensite samples indicate that magnetically attractive domain stripes appear slightly wider than repulsive ones. By scanning one region with opposite tip magnetizations, it can be shown that this asymmetry feature is artificial. The origin lies in an offset of magnetically induced static cantilever deflection. Repulsive forces are limited by the loss of $H_{z,\mathrm{dem}}$ with surface distance, whereas attraction grows with further cantilever bending towards the specimen. Average domain widths λ of experimental and simulated MFM micrographs were taken from the corresponding autocorrelation functions. In case of S1 the value amounts to $\lambda_{\mathrm{MFM}} = 410 \pm 20$ nm in martensite phase. In general, the occurrence of a magnetic domain stripe pattern in thin films is a result of the competition between E_{dem} and E_{mca}. Demagnetization energy E_{dem} —caused by long range dipole-dipole interaction and determined by sample geometry—forces magnetic moments to align properly in order to reduce the overall magnetic stray field energy (e.g., in surface plane for thin films). The short range magneto crystalline anisotropy is mediated by spin-orbit coupling of valence electrons within the lattice and in consequence connected to the orbital electron distribution. This anisotropy can be subdivided into a volume-, a surface-, and a stress part. The surface anisotropy constant exceeds the volume counterpart by far since crystal symmetry at boundaries and surfaces is significantly reduced—an important fact regarding the magnetic behavior of ultrathin films (≤10 nm). If a properly oriented uniaxial magneto crystalline anisotropy is strong enough to face shape anisotropy, a complete alignment of magnetic moments along directions determined by E_{dem} can be prevented. In case of a magneto crystalline easy axis perpendicular to the surface, a domain structure with altering z-magnetization occurs. This pattern tributes to both anisotropy terms and ensures a magnetic alignment along easy axis with low stray field energy at the macroscopic level. Regarding thin films presented here, the easy c_{14M}-axis switches direction periodically with v1 (⊥ surface) and v2 (∥ surface). The influence of this structural feature on the local magnetic structure is addressed later. Simulated data shown in Figure 1b,d represent a qualitative map of relative cantilever phase shift $\Delta\phi_{\mathrm{MFM}}$ due to interaction of sample stray field $\boldsymbol{H}_{\mathrm{dem}}$ with tip magnetization $\boldsymbol{M}_{\mathrm{tip}}$. A tip size of $R_{\mathrm{tip}} = 45$ nm (determined via SEM) including a 30-nm-thick magnetized metal coating and a lift height of $\Delta h = 80$ nm are considered. Based on results given in ref. [8], we chose $K_a = -1.7 \times 10^5$ J m^{-3} and $K_b = -0.9 \times 10^5$ J m^{-3} for magnetic hard axes a_{14M} and medium axes b_{14M}, respectively. A twin variant width of 50 nm, matching the experimental value of S1, was also considered. Concerning the estimation of a proper exchange constant A, we start with a general formulation of spin wave excitation energy $E(k)$[9] in absence of an external magnetic field

$$E\left(\vec{k}\right) = 2S\sum_{\vec{r}} J \ \sin^2\left(\tfrac{1}{2}\vec{k}\cdot\vec{r}\right) \approx \tfrac{S}{2}\sum_{\vec{r}} J \ (\vec{k}\cdot\vec{r})^2 = Dk^2$$

where the approximation holds for long wavelength magnons ($|k| << 1$ Å^{-1}) and D denotes the spin wave stiffness. J is the exchange integral and S defines the magnetic moment. Assuming only nearest neighbor exchange interaction and cubic symmetry, the sum simplifies and one obtains $D = 2\,J\,S\,a^2$ with a being the lattice constant. By small angle neutron scattering, D was determined to be 100 meV Å^2 (austenite) and 150 meV Å^2 (10M martensite).[10] Since the experimentally obtained value of D is approximately constant within $k^2 < 0.025$ Å^{-2},[10] the corresponding parameters J and S may be regarded as effective values over a $L2_1$ Ni-Mn-Ga super cell. With the exchange constant given by $A = J\,S^2\,N/a$[11] one obtains

$$A = \frac{D\,S\,N}{2\,a^3} \tag{1}$$

Assuming the magnetic moment of Mn to be the major contributor to S ($S_{\mathrm{Mn}} = 2.36\ \mu_B$[12] at 293 K in Ni_2MnGa) within the fcc super cell ($N = 4$) of $a = 5.82$ Å in size, Equation 1 yields estimated values alike $A_A \approx 3.8 \times 10^{-12}$ J m^{-1} (austenite) and

$A_{14M} \approx 5.8 \times 10^{-12}$ J m^{-1} - presuming $D_{14M} \approx D_{10M}$ and neglecting an influence of unit cell distortion in modulated martensite. Satisfactory agreement of theoretical and experimental domain structure characteristics is achieved as illustrated in Figure 1a,b. The simulated domain width (390 nm) is close to the experimental value of S1. Varying the hard axis anisotropy constant within 1.0×10^5 J m$^{-3} \leq K_a \leq 1.9 \times 10^5$ J m^{-3}, does not influence the ensemble's relaxation behavior and hence yields similar micromagnetic ground state configurations. This artifact originates from a comparably coarse unit cell size of 10 nm × 10 nm × 10 nm. The contribution of short range exchange interaction, characterized by the exchange length $L_{ex} = \sqrt{AK_i^{-1}} \approx 6 - 12$ nm (depending on literature values), is affected due to inappropriate spin interaction sampling. Simulating a smaller system with increased discretization resolution of 3 nm × 3 nm × 3 nm turned out to be suitable to avoid that relaxation artifact and also smaller variation steps of K_a yield reasonable changes in energetic ground state and domain pattern appearance. However, since computational limitations determine the maximum ensemble discretization to approximately 12 million unit cells, the resulting lateral system extension reduces to only 700 nm in size for a 650 nm thick film allowing no reasonable comparisons with experimentally observed domain widths. The long range character of magnetic dipole-dipole interaction and periodic boundary conditions cause artifacts in simulated domain stripe widths due to self interaction and necessitate the lateral system dimension to be significantly larger than domain width. Nevertheless, simulations with 3 nm unit cell size confirm the applicability of lower discretized simulation boxes in terms of qualitative domain structure comparison and are consulted for domain wall characterization.

For S2, MFM data and topography were acquired at the boundary of neighbored non-patterned and twin-patterned regions (see Figure 1c). Regarding the latter one, corresponding magnetic domain structure appears more disturbed compared to S1. We address this phenomenon to a higher structural and magnetic disorder. The structural disorder includes a more pronounced rhombohedral superstructure of twin pattern due to variant branching and an increased twin variant width fluctuation. Moreover, the average twin variant width of S2 only amounts to 25 nm. Magnetic disorder should be caused predominantly by local variations of magneto crystalline anisotropy. A locally fluctuating in-plane stress state, caused by preparation conditions of S2 mentioned before, is most probably responsible for such disorder artifacts. The non-patterned region of S2 shows narrow stripes with a magnetic response perpendicular to surface. These stripes are separated by broad bands possessing only poor out-of plane magnetization. At the boundary to the twin patterned region, narrow stripes coincide with 180° domain walls. The crystal structure of these non-patterned regions of S2 was previously determined to be oriented anomalously, having b_{14M} axis normal to film plane[13] and possessing *a*-*c*-twinning within the surface. This is in accordance to earlier work, stating that b_{14M} axis is aligned normal to surface[14] and coexistence of both twinning orientations[15] can occur.

Consequently, narrow magnetic stripes should represent 180° domain walls of magnetic domain stripes which in turn are aligned to the $[101]_A$ direction. Considering these crystallographic features in the simulation reveals a similar MFM micrograph (see Figure 1d). The average domain stripe width amounts to 310 ± 5 nm and matches the experimental value (λ_{MFM} = 290 ± 30 nm) well. A 135° kink occurs between domain walls of patterned and non-patterned regions.

This feature cannot arise if the non-patterned region would be solely a single variant state with magnetic easy c_{14M} axis in surface plane since domain walls of both regions would be in parallel.

Concerning the non-patterned region, simulation shows domain walls having +*z* and −*z* orientation whereas experimental MFM data only show an attractive out-of-plane magnetization component being slightly interrupted at several positions. This discrepancy might originate from the fact that the computational approach assumes two free surfaces. In case of real Ni-Mn-Ga thin films, one surface is constrained by the substrate, manifesting in stresses and a deviation from 14M martensite crystal structure close to the MgO interface. Moreover, simulated stray field minimization is realized within a very limited volume, whereas the real demagnetization energy of the large extended specimen is not affected considerably by magnetic states of micrometer-sized regions, allowing one preferential orientation. In this context, the question about influences of nano-twinning on domain structure as well as domain wall type appearance arises.

Magnetization vector fields of three films with similar thickness of 640 nm were simulated considering lateral twin variant sizes of 2000, 400, and 50 nm respectively. Starting with the largest variant extension of 2000 nm, different magnetic patterns form out within the two variants (see **Figure 2**a). In v_1, where the easy *c* axis is normal to surface plane, an angular disordered two-domain pattern with alternating M_z components occurs. Variant v_2 exhibits an in-plane two domain stripe configuration—aligned perpendicular to twin boundaries—with alternating M_y component and separated by domain walls with poor out-of-plane magnetization. As described previously for S2, they also partially coincide with domain walls of v_1. The average domain width in v_2 is larger than in v_1. In both variants, the simulation predicts a depth dependence of domain wall characteristics. At the surface, domain walls exhibit a Néel-like spin reorientation within v_1 and a cross-tie behavior in v_2 (not shown here) due to flux closure tendencies in order to reduce stray field energy.[16] Proceeding along *z*-direction, buried layers show a continuous transition to Bloch-like spin realignment until a pure Bloch wall is prevalent. The pattern formation process is affected when decreasing variant size to 400 nm (see Figure 2b). Analogue magnetic structures still manifest but the number of coinciding domain walls at neighbored variants increases. Moreover, the average domain width in v_2 decreases, whereas only minor changes are obtained in v_1. Finally, the micromagnetic structure at 50 nm twinning distance is shown in Figure 2c. Domain morphology appears as an ordered stripe pattern with out-of-plane magnetization distributed homogeneously over the whole simulation cell. Considering the cross sectional view (along black solid line in Figure 2c), magnetic moments in v_1 are not aligned perfectly with easy c_{14M} axis but have an average altitude angle of about 45° (disregarding closure effects at surfaces). MFM measurements at a low lift height of 20 nm show a similar magnetic modulation along

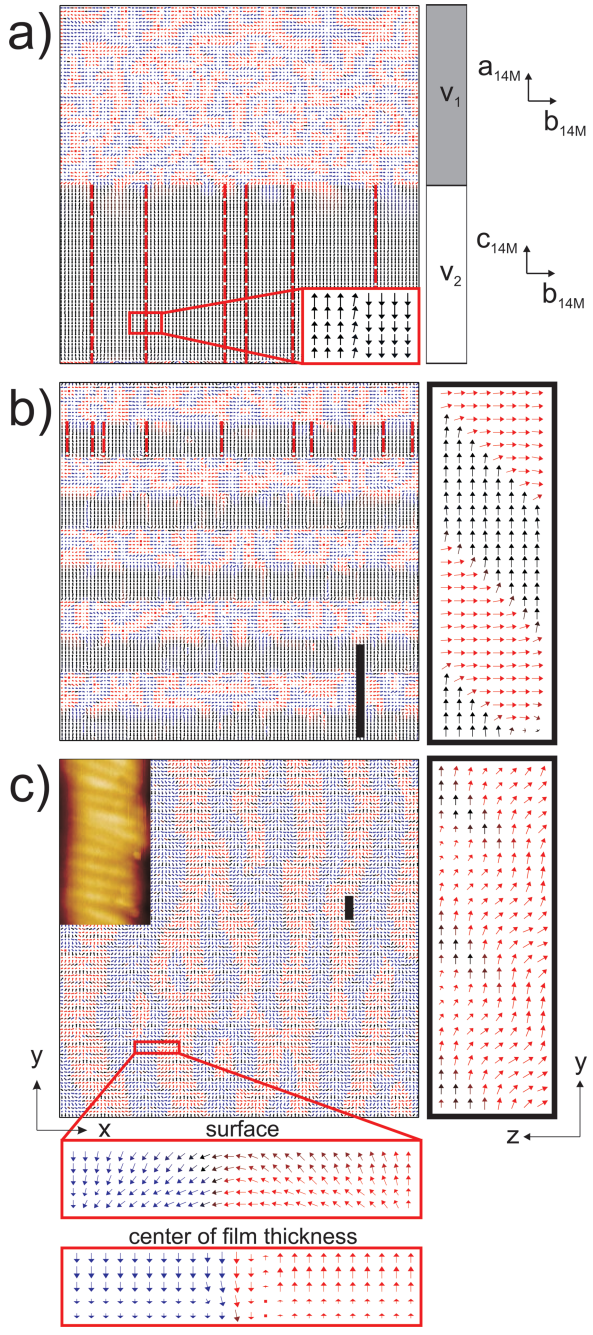

Figure 2. Simulated magnetization vector fields for three twin variant widths, a) 2000 nm, b) 400 nm and c) 50 nm. Red dashed lines in v_2 indicate positions of domain walls. Red boxes are magnifications of red framed sections and black boxes in b) and c) show cross sectional views along the black lines. Unit cell size is 10 nm^3 and arrow spans are 40 nm (top views, cross section b)) and 10 nm (cross section c)). For comparison, an MFM image inset is given in (c).

domain stripes as can be seen in the inset of Figure 2c. What initially might be interpretable as imaging artifact due to the twin patterned surface topography, turns out to be a real magnetic fine structure by comparing trace and retrace MFM scans as well as repeated measurements at 180° sample rotation. The angular spin misalignment, mentioned before, is caused by the dipole field of magnetic poles located at twin boundaries to neighboring v_2 variants. The field strength rises with reduction of lateral variant extension and gets important once nanotwinning occurs.

2.2. Temperature Dependent MFM Measurements

As exemplarily illustrated for the MFM-temperature cycle in **Figure 3**, increasing film temperature close to the martensite-austenite transition causes a smoothing of topography and the characteristic twin variant pattern nearly vanishes ($\Delta h_{RMS} \approx 0.5$ nm). This structural transition, however, initiates locally within microscopic regions (Figure 3, 302 K) and proceeds by further heating to 308 K until the whole sample surface is smoothed out. The temperature interval at which this gradual transition occurs amounts to $\Delta T \approx 5 \pm 2$ K, very similar to the temperature hysteresis of TDRC. However, a remnant twin-like corrugation pattern still remains over the entire sample, independent of temperature. This residual surface feature could either originate from (i) highly ordered lattice defects at twin boundaries generated during the first martensite transition after film deposition, (ii) a remnant martensite probably located close to surface or (iii) an oxide-layer growing on top of the twin-patterned surface right after first air exposure. The surface oxidation may preferentially proceed at twin boundaries or one of both variants, resulting in an oxide layer resembling the footprint of the characteristic twin pattern. Rutherford backscattering spectrometry (RBS) data yield an oxygen content of typically $11 \pm 0.5 \times 10^{15}$ atoms cm^{-2} at the surfaces of presented samples. Assuming a predominant formation of Mn_xO_y[17] this amount corresponds to an approximately 2 nm thick metal oxide surface layer. Together with the fact that no such residual pattern is observable on the austenite sample S3 (no martensite transition prior to first air exposure but during TDRC acquisitions) favors assumption (iii). However, at the phase transition the average phase shift $\Delta\phi_{MFM}$ between neighbored stripe domains drops by a factor of 7 ± 1.5 and an abrupt change in average domain width is observed ($\lambda_{A1} \approx 360 \pm 10$ nm). Additionally, the pattern disorder increases.

Further heating slightly below 338 K steadily reduces magnetic phase contrast down to $\Delta\phi_{MFM} = 0.3° \pm 0.1°$. At a sample temperature of 338 K a collective magnetic domain reconfiguration occurs. The new domain pattern, denoted as A2, is characterized by a strong asymmetry of domain stripe thickness (bright attractive domains appear about four times broader than dark ones), whereas the average domain stripe thickness reduces down to $\lambda_{A2} = 290 \pm 20$ nm (about 100 nm smaller than in the martensite phase). Moreover, a reorientation of the magnetic domain ensemble occurs. In case of the MFM cycle shown in Figure 3, domains align to the $[110]_A$ direction. At around 340 K, this structure fades out and an even weaker, coarse and diffuse magnetic pattern (A3) appears. Finally, above 343 K no MFM response is observable anymore, despite the fact that S1 is still ferromagnetic. After further heating beyond the Curie temperature, MFM measurements are repeated during a cooling cycle. Starting at 340 K, one again observes the appearance of the weak diffuse magnetic structure A3 and about 2 K below, A3 transforms back into A2 yielding

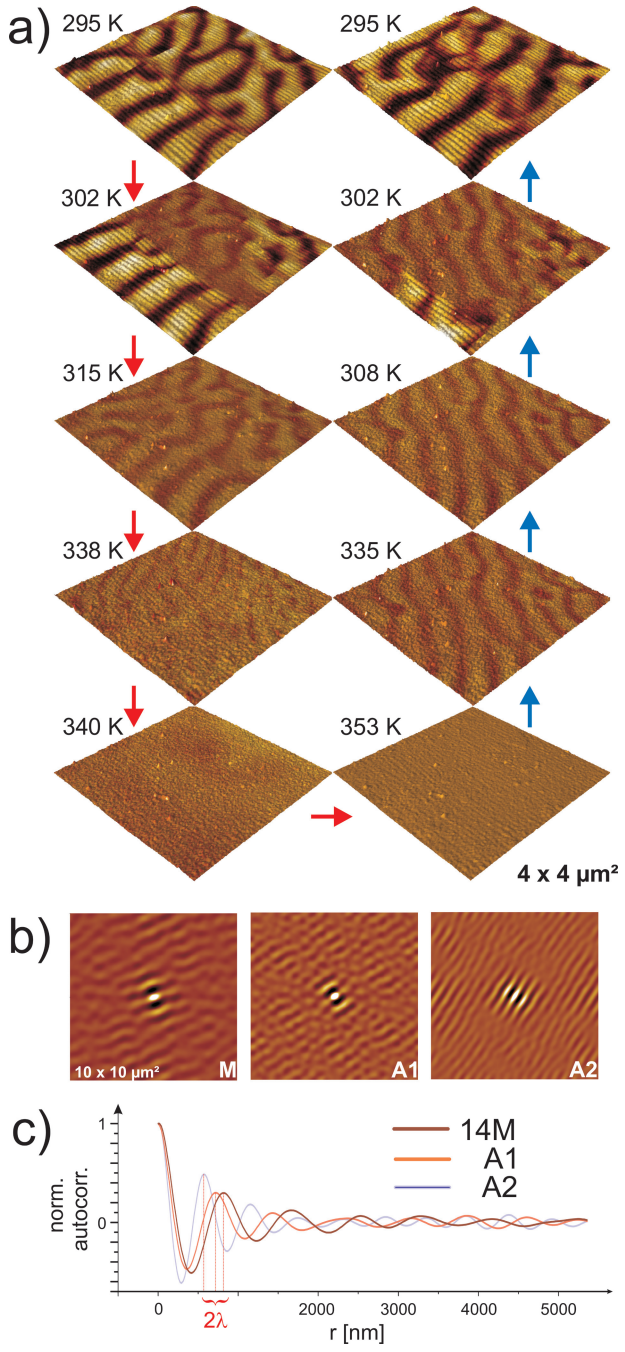

Figure 3. a) 4 µm × 4 µm cutouts of 10 µm × 10 µm MFM micrographs of S1 for one heating-cooling-cycle showing the typical domain stripe pattern (M) in 14M martensite at 295 K, A1 within 302 K ≤ T < 338 K upon heating, A2 within 335 K ≥ T ≥ 302 K upon cooling and A3 at 340 K. b) Autocorrelation functions of MFM phase contrast images. c) Normalized cross sections of autocorrelation functions yield information about domain stripe widths λ.

again a high domain width asymmetry (not shown for the cooling cycle). At 335 K, no remarkable asymmetry is observable anymore and the average domain thickness of A2 remains constant at λ_{A2} = 290 ± 10 nm. Further lowering the sample temperature down to 308 K only increases the MFM phase contrast $\Delta\phi_{MFM}$. Approaching the structural transition temperature towards martensite phase, a twin variant pattern arises locally again and MFM phase response increases discontinuously within these regions accompanied by a magnetic domain stripe reorientation back along $[100]_A$ direction and domain width enlargement to its initial value of about 410 nm. The twin pattern forms first within the same regions where it vanished last during heating. At this point, it should be noted that the experimental procedure described above was applied to several positions of S1, S2, and S3. Concerning these experiments, we first need to summarize corresponding findings before starting with a discussion. As discussed in the previous section, a small asymmetry of domain stripe width in the martensite phase at room temperature was found to be a measuring artifact. The much more pronounced width of magnetically attractive domains in A2 at elevated temperatures close to the Curie point (Figure 3 at 338 K), however, can probably be attributed to magnetic reorientations in presence of the tip's stray field due to increased entropic influence and lower coercivity fields arising in the austenite phase. Alignment tendencies of the A2 pattern along $[110]_A$ were observed at multiple regions of S1, with corresponding MFM micrographs yielding up to 20° angular deviation. In some regions, however, alignment was along $[100]_A$.

No recognizable correlations to macroscopic measuring position (e.g., center, edges, corners of sample) were found. Moreover, the alignment of domain pattern during austenite-martensite transition did not necessarily end up perfectly perpendicular to twin pattern corrugation lines but deviations up to 20° even at length scales of several tens of micrometers were observed.

Absence of any domain pattern could be obtained in austenite S2 since the structural transition at T_{MA} = 344 K appears to be too close to the Curie point. Regarding S3, we were not able to acquire MFM data in the martensite phase, since the sample holder does not allow cooling below 275 K. Prior to the first TD-MFM cycle, the austenite phase, however, also reveals a well pronounced and highly ordered domain stripe pattern (λ_{A2} = 200 nm) at room temperature being aligned with the $[100]_A$ direction. Angular orientation of the pattern becomes slightly more disturbed after several heating-cooling cycles beyond the Curie temperature but average domain stripe width keeps constant. Summarizing all experimental findings described above, the TD-MFM experiments reveal three remarkable findings: (i) there is an abrupt drop of $\Delta\phi_{MFM}$ and λ at the structural phase transition and a magnetic domain stripe pattern A1 remains in the austenite phase; (ii) there is a certain temperature where magnetic domain structure changes from A1 to A2 within austenite phase, which means that the average domain stripe width reduces and a change in angular orientation occurs; (iii) the occurrence of both metastable patterns, A1 and A2, shows a temperature hysteresis. The pattern A1 appears approximately within T_{MA} < T < 338 K if initial temperature is below martensite-austenite transition T_{MA}. Domain pattern A2 condenses above 338 K and remains stable between T_{MA} < T < 340 K, being therefore energetically more stable than A1. Suggestions dealing with the two last mentioned findings are given at the end of this discussion. Addressing finding (i), the abrupt phase drop originates from the lattice reconfiguration

towards fcc structure, which especially reduces the magneto crystalline anisotropy and leads to a more pronounced flux closure at sample surfaces with predominant in-plane magnetization. Assuming the ideal case, a transition from 14M martensite to austenite is coupled to a change from orthorhombic to cubic magneto crystalline anisotropy. Since corresponding anisotropy constants are reported to be 10^2–10^3 times lower than their counterparts in martensite[18,19] and due to symmetry, no domain stripe pattern with detectable out of plane magnetization should arise in perfect unstressed austenite thin films. This is confirmed by OOMMF simulations. One critical influence not considered up to now within the micromagnetic simulations is the mechanical stress arising in epitaxially-grown thin films. Besides the volume magneto crystalline anisotropy, a stress induced anisotropy term can arise in strained systems. Moreover, the Mn-rich off-stoichiometric composition might affect magneto crystalline anisotropy too. It is therefore important to know the stress/strain state of austenite thin films deposited on MgO and whether corresponding magneto crystalline anisotropy is sufficient to be the primary cause of the domain stripe pattern observed experimentally. Concerning film deposition by magnetron sputtering, it was shown[20] that an island-like growth occurs during the first nanometers and tensile stresses arise due to subsequent island coalescence as well as a lattice mismatch of 2.3%. Once the thin film closes (≈5 nm thickness), compressive stresses due to atomic peening get dominant, viz. an excess densification of the film due to energetic impacts during sputter deposition e.g., via interstitial creation. The stress state remains nearly constant over film thickness as long as sputter deposition continues. Elevated substrate temperatures around 900 K promote stress relaxation after deposition by Frenkel pair recombination within the film and defect annihilation at surface/film-substrate interface, respectively. Remaining compressive in-plane stresses are intrinsic and reported to be lower than 50 MPa.[20] During first sample cooling, tensile stress due to different thermal expansion of film and substrate occurs. Approaching the martensite transition, this stress state is effectively reduced by twinning and recovers again when performing austenite transition.[21] The question about how stress is predominantly moderated in Ni-Mn-Ga thin films, either by defect generation or pure elastic straining, was the subject of previous research.[22] The latter is favored due to several facts such as the occurrence of a magnetic domain pattern in the austenite phase, similar resistivity curves upon repeated heating and cooling cycles (no significant shift in martensite transition temperature) and a reversible stress accumulation/relaxation during forward and reverse phase transitions reported in ref. [21]. Assuming thermal expansion coefficients of $\alpha_{Ni-Mn-Ga} = 15 \times 10^{-6}$ K^{-1}[23] and $\alpha_{MgO} = 10.8 \times 10^{-6}$ K^{-1}[24] as well as $\Delta T = T_{depos} - T_{room} = 900$ K $-$ 293 K = 607 K yields a nominal in-plane lattice strain of $\varepsilon = 0.26\%$. Although $\alpha_{MgO}(T)$ is known in a wide temperature interval,[25,26] no corresponding data is available for austenite Ni-Mn-Ga up to now, forcing us to regard the result as a rough estimation. In principle, another way to estimate an in-plane strain is based on a Clausius-Clapeyron approach which utilizes the temperature shift ΔT_{MA} of martensite-austenite transition compared to bulk material with the same chemical composition. The considerable error of ΔT_{MA}, however, originating from uncertainties of the utilized phase diagram[27] as well as chemical compositions amounts to ±40 K and results in thermal stress uncertainties of ±90 MPa (using $d\sigma/dT_{MA} = 2.2$ MPa K^{-1}).[28–30]

This result hardly allows any reasonable comparison between films of different composition. Following experimental results based on X-ray stress analysis measurements,[31] the biaxial thermal in-plane stress is $\sigma_{therm} \approx 100$ MPa. Basically, the corresponding strain is calculable with known elastic properties of austenite Ni-Mn-Ga. However, since mechanical response in general, and especially in case of FSM alloys, highly depends on probing frequency and the amount of applied strain specific for a certain measuring technique, values of Young's modulus given in literature vary considerably. Assuming a biaxial modulus of $M = E/(1-\nu) \approx 40$ GPa for Ni-Mn-Ga,[23,32] one finally obtains $\varepsilon = 0.25\%$ close to the value calculated with known thermal expansion coefficients. Due to symmetry of elastic behavior of austenite Ni-Mn-Ga ($C_{11} \approx C_{22} \approx C_{33}$) the estimated in-plane lattice strain of $\varepsilon \approx 0.25\%$ causes a contraction in vertical dimension (tetragonal distortion) and it is plausible that an uniaxial magnetic easy axis in z-direction occurs. Although no detailed magnetic study of presented samples is available so far, first magnetization measurements reveal an out-of-plane coercivity field H_c which clearly exceeds the in-plane value. This fact supports the suggestion of a stress-induced magneto crystalline anisotropy.

An attempt to estimate K_{stress} is discussed as follows. The total magnetic energy of a simplified two-dimensional model system is calculated analytically according to ref. [16]. As illustrated in **Figure 4**a the model assumes a continuous transition

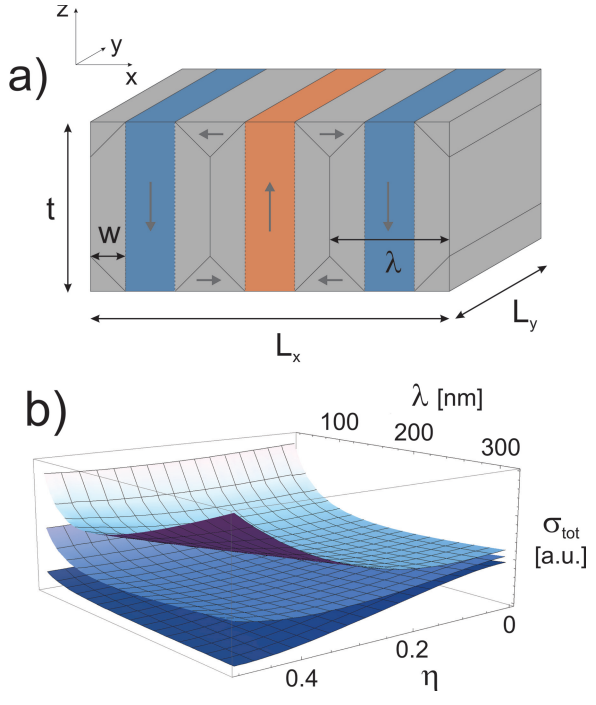

Figure 4. a) Scheme of the modeled magnetization distribution with partial flux closure. b) Total areal magnetic energy density landscapes σ_{tot} vs. domain width λ and relative flux closure constant η for $K_{stress} = 2 \times 10^5$ J m^{-3} (top layer), 5×10^4 J m^{-3} (middle layer) and 5×10^3 J m^{-3} (bottom layer).

from an open flux domain stripe configuration to a fully closed state via increasing partial flux closure domains (Néel caps). These regions defined by the cap width 2 w (grey colored areas in Figure 4a) do not have accumulative magnetic pole strength and therefore do not contribute to the demagnetization energy density σ_{dem}. The total magnetic energy per unit area $\sigma_{tot} = E_{tot}/(L_x L_y)$ is written as

$$\sigma_{tot} = \sigma_{dem} + \sigma_{stress} + \sigma_{wall} \quad (2)$$

where σ_{dem} is determined by $\int_0^{-t} \boldsymbol{M}\,\boldsymbol{H}\,dz$ with the given periodic magnetic pole distribution $\boldsymbol{M}(x, z)$ in Figure 4a (described by its Fourier expansions) and $\boldsymbol{H}$ as solution of the Laplace equation:[16,33]

$$\sigma_{dem} = \frac{\mu_0 M_s \lambda}{\pi} \sum_{\substack{n=-\infty \\ n\neq 0}}^{n=\infty} \frac{C_n(\eta) C_{-n}(\eta)}{|n|} \quad (3)$$

M_s denotes the saturation magnetization and λ describes the domain width as depicted in Figure 4a. The Fourier coefficients $C_{\pm n}$ of normalized $\boldsymbol{M}(x, z)$ depend on η: $= w/\lambda$, which describes the relative size of flux closure caps with respect to the stripe domain width. It varies between 0 (no flux closure) and 0.5 (complete closuring). The stress induced anisotropy energy per unit area σ_{stress} arises within flux closure caps since magnetic moments are oriented perpendicular to the easy axis along z-direction and amounts to

$$\sigma_{stress} = 2\ K_{stress}\ \eta^2 \lambda \quad (4)$$

Finally, the Bloch wall energy contribution σ_{wall} at neighboring stripe domains is given by

$$\sigma_{wall} = \sigma_{ex}\left(\frac{t}{\lambda} - 2\eta\right) \quad (5)$$

with areal exchange energy density $\sigma_{ex} = 4\sqrt{AK_{stress}}$. An additional wall energy contribution from realigning moments at cap domain boundaries is omitted here. Strictly speaking, flux closure caps are basically Néel-like 180° walls with an average lateral extension in the order of $w >> L_{ex}$ and contribute a minor part to exchange energy. This might lead to an overestimation of σ_{stress} since spins are not perfectly aligned with surface plane as idealized here, but have an out-of-plane component. Their consideration, however, would cause additional adjustable parameters besides η being hardly accessible by experiments. In Figure 4b, the total magnetic energy landscape $\sigma_{tot}(\eta, \lambda)$ is plotted for three different K_{stress} values. As can be seen therein, the occurrence of local minima apart from trivial solutions at $\eta = 0$ (no flux closure) and $\eta = 0.5$ (complete closuring) is only fulfilled within 10^4 J m^{-3} $\leq K_{stress} \leq 1.5 \times 10^5$ J m^{-3}. Considering the given experimental values λ_{A2} and t of S1 and S3 (see Table 1), the minimization of $\sigma_{tot}(\eta, \lambda)$ with respect to (η, λ) yields $K_{stress} \approx 1.4 \times 10^4$ J m^{-3} at $\eta = 0.47$ (S1) and $K_{stress} \approx 1.6 \times 10^4$ J m^{-3} at $\eta = 0.46$ (S3). This result states that flux closure proceeded strongly, but not completely, in both films, which goes hand in hand with the pronounced drop in relative MFM phase shift $\Delta\phi_{MFM}$ between neighboring domains during austenite transition. The linear correlation of $\Delta\phi_{MFM}$ with the force gradient caused by $\partial H_z/\partial z$, which in turn changes proportionally with M_z, allows an estimation of η by comparing $\Delta\phi_{MFM}$ in martensite and austenite. Assuming the phase response to originate only from the non-closed domain fraction and its lateral dimension to be small compared to R_{tip} (which should be the case for high η), one obtains $\eta_{MFM} = ½\ (1 - \Delta\phi_{A2}/\Delta\phi_{14M}) \approx 0.43$. This value represents a lower limit since spins in twinned martensite are not perfectly aligned out-of-plane as discussed in the previous section. Considering a misalignment angle of 45° according to micromagnetic simulations yields $\eta_{MFM} = 0.45$, agreeing fairly well with values calculated analytically. Finally, determined values of K_{stress} based on this rather simplified model system are supported by OOMMF simulations which predict a domain stripe pattern condensation with out-of-plane magnetization above 8×10^3 J m^{-3}. The stress-induced magneto crystalline anisotropy constant in our thin films is therefore assumed to be located within the low 10^4 J m^{-3} regime. The occurrence of metastable domain configurations A1 and A2 leads to a consideration of findings (ii) and (iii). Referring again to Figure 4b and focusing on the energy landscape propagation along λ-axis at a given η, decreasing K_{stress} is coupled to a surface curvature reduction (smooth landscape) and thus to a less pronounced energetic minimum E_{min}. The actual value of E_{min} depends consequently more critical on influences like thermal disordering, not considered in this model. The presence of multiple shallow minima is thinkable. As a result, the formation of a certain micromagnetic domain configuration is considerably affected by further parameters such as the initial ensemble state and more complex variations of magneto crystalline anisotropy with temperature.

3. Conclusions

A comparison between experimental and simulated micromagnetic structure was given for epitaxial 14M modulated martensite Ni-Mn-Ga thin films on MgO substrates. This procedure allows a non-destructive determination of local crystal orientation. The computational approach used here predicts the influence of sample thickness on domain stripe width correctly. The lateral twin variant size was varied in order to investigate its impact on magnetic domain structure formation from a theoretical point of view. Flux closure tendencies due to the demagnetization field strength at film surfaces cause a transition of domain wall type with depth. Temperature dependent MFM measurements in the proximity of structural transition temperature and beyond reveal the existence of a domain stripe pattern with detectable out-of-plane magnetization in the parental austenite phase. An uniaxial magneto crystalline anisotropy K_{stress} with easy axis out-of-plane—induced by biaxial thermal stresses—might be the primary cause. The appearance of two metastable micromagnetic domain patterns within an overlapping temperature window could be correlated to an interplay of the shallow total magnetic energy landscape in stressed austenite Ni-Mn-Ga and the raising entropic influence close to Curie temperature. Further studies are required to treat this topic more thoroughly.

Temperature dependent studies of lattice distortion via XRD as well as magneto crystalline anisotropy by further magnetization measurements in austenite Ni-Mn-Ga thin films on MgO are a next step. Similar MFM measurements on lift-off films are necessary in order to verify presumptions mentioned here

Table 1. Selected properties of samples S1–S3. The relative concentration errors among samples are due to peak fitting uncertainties of PIXE analysis software and amount to 0.6% (Ni), 0.6% (Mn) and 1% (Ga) which allows the comparison of electron per atom ratios e/a with an accuracy of ±0.03. The relative error of absolute elemental composition is, however, 2%.

Sample	Elemental composition	t	T_{MA}	T_{AM}	T_C	e/a	λ_{14M}	λ_A
	[at%]	[nm][a)]	[K]	[K]	[K]		[nm]	[nm]
S1	$Ni_{48.3\pm0.2}Mn_{31.0\pm0.1}Ga_{20.7\pm0.2}$	640 ± 15	307 ± 1	304 ± 1	363 ± 2	7.62 ± 0.03	410 ± 20	290 ± 10
S2	$Ni_{49.2\pm0.3}Mn_{30.7\pm0.2}Ga_{20.1\pm0.2}$	375 ± 10	344 ± 1	339 ± 1	359 ± 2	7.67 ± 0.03	290 ± 10	–
S3	$Ni_{47.7\pm0.3}Mn_{30.4\pm0.2}Ga_{21.9\pm0.2}$	312 ± 10	265 ± 1	258 ± 1	366 ± 2	7.56 ± 0.03	–	215 ± 10

[a)]calculated from RBS areal mass density σ_{md} ([mg cm^{-2}]) data assuming $\rho \approx 8000$ kg m^{-3}.

and to gain information about the influences of off-stoichiometric composition and intrinsic stresses. Additionally, a determination of magneto-elastic coupling constants via first principles simulations is desirable to allow the estimation of K_{stress} by a magnetostrictive approach.

4. Experimental Section

Sample Preparation: Ni-Mn-Ga thin film samples (which we enumerate with S_i, $i = 1, 2...$ in the following) were grown on MgO (100) substrates (10 mm × 10 mm × 0.5 mm) by magnetron sputter deposition from a multicompound target, similarly as described before.[17] Prior to deposition, the chamber was baked for at least 8 h to ensure a base pressure within the high vacuum (HV) regime and to dehydrate the MgO substrate. After a pre-sputtering period, films of different thickness were deposited at 900 K substrate temperature and a deposition rate of 0.19 nm s^{-1} using an Ar pressure of 3×10^{-3} mbar. Nominal sputtering power was 50 W (DC). Samples were routinely checked for their crystal structure and epitaxial quality using X-ray diffractometry (XRD). For the deposition process of S2, a wedge was mounted below one substrate side causing only the clamped edge to be in direct contact with the sample heater. This configuration in turn caused the appearance of microscopic regions which yield a flat surface morphology rather than the typical twin corrugation pattern. These stripe-like areas are a few micrometers wide, up to 100 µm long and occurred only close to the clamped substrate edge. Temperature- and stress gradients correlated to this mounting are probably the origin. Details of the physical properties of S1–S3 can be taken from **Table 1**.

Micromagnetic Simulations: In order to examine magnetic structure formation from a theoretical point of view, we performed micromagnetic simulations utilizing the Object Oriented MicroMagnetic Framework (OOMMF) code.[34] For direct comparisons to experimental data, the thickness of Ni-Mn-Ga thin films, cantilever lift height and tip dimensions were considered, whereas the lateral simulation box dimension was chosen as large as possible within the computational limits (4 µm × 4 µm in *x*-*y*-surface plane at 10^3 nm^3 unit cell resolution and 0.8 µm × 0.8 µm at 3^3 nm^3). The unit cell resolution was varied depending on the focus of interest as explained in the Discussion. Contributors to the ensemble's total magnetic energy E are the exchange term E_{ex} described by a uniform exchange constant A [J m^{-1}], the magneto-crystalline anisotropy energy E_{mca} characterized by uniaxial anisotropy constants K_i [J m^{-3}] as well as the demagnetization term E_{dem}. The minimization of E was realized using a conjugated gradient evolver (CGE). Exemplary systems were modeled considering the film thickness as well as phase appearance (properly chosen values of K_i for 14M martensite from literature) and local crystal orientation due to twinning. If not declared otherwise, two dimensional periodic boundary conditions were assumed in surface plane to address the thin film character of our samples.[35]

Sample Characterization: Temperature dependent resistivity curves (TDRC) were acquired with a Quantum Design Physical Property Measuring System in order to gain structural transition temperatures T_{MA} (martensite → austenite) and T_{AM} (austenite → martensite) as well as the Curie temperature T_C. The measurements were realized by a four-point probe contact, whereas resistivity R at a certain temperature T was determined from an average over 25 *I*–*U* curves. Temperature steps were chosen to be $\Delta T = 1$ K and T was automatically stabilized prior to each data acquisition with an accuracy of $\Delta T = 0.05$ K. Elemental composition as well as depth homogeneity and film thickness t were determined with particle induced X-ray emission (PIXE) and Rutherford backscattering spectrometry (RBS) experiments. PIXE measurements were conducted with 2.03 MeV protons whereas RBS was realized using He^+ ions of the same kinetic energy. A sample tilt angle of 5° was chosen to avoid channeling artifacts. PIXE was chosen due to its superior detection limit of elements compared to energy dispersive X-ray spectroscopy (EDX), allowing more accurate comparisons of elemental contents of thin films. Magnetic force microscopy (MFM) micrographs of 4 µm × 4 µm and 10 µm × 10 µm in size were acquired within a temperature range of 295 K ≤ T ≤ 375 K for all samples in absence of an external magnetic field. An Asylum Research MFP-3D AFM[36] equipped with a Cr/Co-coated Bruker MESP cantilever (≈400 Oe coercivity field, tip radius $R_{tip} = 45$ nm) was used for this purpose. Temperature control was realized by a self-constructed sample holder with an accuracy of 2 K. The MFM tip—magnetized perpendicular to sample surface (*z*-direction)—first performed a line scan in AC (tapping) mode (surface characterization) and subsequently followed this surface profile with a constant vertical lift height. During this second non-contact scan, cantilever resonance frequency shifts due to interaction with the sample's magnetic stray field. This shift is acquired indirectly by mapping phase changes between excitation- and cantilever frequency since direct resonance frequency tracking is connected with higher efforts and time consumption. According to ref. [37], low frequency shifts are approximately proportional to the convolution of $M_{z,tip}$ and the second partial derivative of sample's demagnetization field $\partial^2 H_{z,dem}/\partial z^2$ over tip volume. We therefore post-processed simulated stray fields $\boldsymbol{H}_{dem}$ in order to gain theoretical MFM frequency shift micrographs, allowing a qualitative comparison to experimental MFM results. This numerical approach considers $\boldsymbol{M}_{tip}(x, y, z)$ of the magnetized tip coating as well as tip-surface distance and follows the procedure described in ref. [37].

Acknowledgements

We appreciate the general support of Prof. B. Rauschenbach. Furthermore, we owe thank to F. Schmidt and Prof. M. Grundmann (Semiconductor Physics Group, Faculty of Physics and Earth Sciences,

University of Leipzig) for conducting initial TDRC. Our gratitude is expressed to Dr. M. J. Donahue (Mathematical & Computational Sciences Division at NIST, Gaithersburg) for considerate initial support concerning OOMMF simulations. Useful discussions with A. Landgraf and J. Buchwald are gratefully acknowledged. This work was funded in parts by the German Federal Ministry of Education and Research (BMBF), PtJ-Bio, 1315883, the Leipzig Graduate School of Natural Sciences BuildMoNa established by the German Science Foundation (DFG) and the SAW award of the German Leibniz Association (SAW-2011-IOM-2).

Received: January 15, 2013
Revised: February 27, 2013
Published online: April 25, 2013

[1] V. V. Kokorin, V. A. Chernenko, *Fiz. Met. Metalloved* **1989**, *6*, 1157–1161.
[2] V. A. Chernenko, E. Cesari, V. V. Kokorin, I. N. Vitenko, *Scr. Metal. Mater.* **1995**, *33*, 1239–1244.
[3] K. Ullakko, *J. Mater. Eng. Perform.* **1996**, *5*, 405–409.
[4] V. A. Chernenko, M. Ohtsuka, M. Kohl, V. V. Khovailo, T. Takagi, *Smart Materials and Structures* **2005**, *14*, S245–S252.
[5] A. Backen, S. R. Yeduru, M. Kohl, S. Baunack, A. Diestel, B. Holzapfel, L. Schultz, S. Fähler, *Acta Mater.* **2010**, *58*, 3415–3421.
[6] V. A. Chernenko, R. Lopez Anton, M. Kohl, M. Ohtsuka, I. Orue, J. M. Barandiaran, *J. Phys.: Condens. Matter* **2005**, *17*, 5215–5224.
[7] A. Diestel, A. Backen, V. Neu, L. Schultz, S. Fähler, *Scr. Mater.* **2012**, *67*, 423–426.
[8] L. Straka, O. Heczko, *J. Appl. Phys.* **2003**, *93*, 8636.
[9] Neil W. Ashcroft, N. D. Mermin, *Solid State Physics*, Holt, Rinehart and Winston, New York **1976**.
[10] V. Runov, U. Stuhr, *J. Magn. Magn. Mater.* **2011**, *323*, 244–247.
[11] H. Kronmüller, in *Moderne Probleme der Metallphysik*, *vol. 2* (Ed: A. Seeger), Springer, Berlin **1966**), p. 24.
[12] M. Kallmayer, P. Pörsch, T. Eichhorn, H. Schneider, C. A. Jenkins, G. Jakob, H. J. Elmers, *J. Phys. D: Appl. Phys.* **2009**, *42*, 084008.
[13] A. M. Jakob, M. Müller, B. Rauschenbach, S. G. Mayr, *New. J. Phys.* **2012**, *14*, 033029.
[14] T. Eichhorn, R. Hausmanns, G. Jakob, *Acta Mater.* **2011**, *59*, 5067–5073.
[15] C. A. Jenkins, R. Ramesh, M. Huth, T. Eichhorn, P. Pörsch, H. J. Elmers, G. Jakob, *Appl. Phys. Lett.* **2008**, *93*, 234101.
[16] C. Kittel, *Rev. Mod. Phys.* **1949**, *21*, 541–583.
[17] G. J. Mahnke, M. Seibt, S. G. Mayr, *Phys. Rev. B* **2008**, *78*, 012101– 012104.
[18] R. Tickle, R. D James, *J. Magn. Magn. Mater.* **1999**, *195*, 627–638.
[19] O. Heczko, J. Kopecek, D. Majtas, M. Landa, *J. Phys.: Conf. Ser.* **2011**, *303*, 012081.
[20] G. J. Mahnke, *Diploma Thesis, Georg-August-Universität, Göttingen* **2008**.
[21] S. Besseghini, A. Gambardella, V. A. Chernenko, M. Hagler, C. Pohl, P. Mullner, M. Ohtsuka, S. Doyle, *Europ. Phys. J.: Spec. Top.* **2008**, *158*, 179–185.
[22] V. A Chernenko, M. Kohl, M. Ohtsuka, T. Takagi, V. A. L'vov, V. M. Kniazkyi, *Mat. Sci. Eng. A* **2006**, *438–440*, 944–947.
[23] St. Besseghini, T. Cavallin, V. Chernenko, E. Villa, V. Lvov, M. Ohtsuka, *Acta Mater.* **2008**, *56*, 1797–1801.
[24] Crystran Ltd. http://www.crystran.co.uk.
[25] R. Reeber, K. Goessel, K. Wang, *Eur. J. Mineral* **1995**, *7*, 1039–1047.
[26] L. S. Dubrovinsky, S. K. Saxena, *Phys. Chem. Minerals* **1997**, *24*, 547–550.
[27] A. Planes, L. Manosa, A. Saxena, *Magnetism and Structure in Functional Materials*, volume *79* of Springermaterials. Springer-Verlag, Berlin **2005**.
[28] M. P. Baron, M. Morin, *J. Phys. IV* **1997**, *07:C5*, 525–530
[29] V. A. Chernenko, V. L'vov, J. Pons, E. Cesari, *J. Appl. Phys.* **2003**, *93*, 2394.
[30] V. A. Chernenko, J. Pons, E. Cesari, K. Ishikawa, *Acta Mater.* **2005**, *53*, 5071–5077.
[31] M. Thomas, O. Heczko, J. Buschbeck, L. Schultz, S. Fähler, *Appl. Phys. Lett.* **2008**, *92*, 192515.
[32] S. Doyle, V. A. Chernenko, S. Besseghini, A. Gambardella, M. Kohl, P. Müllner, M. Ohtsuka, *Europ. Phys. J.: Spec. Top.* **2008**, *158*, 99–105.
[33] An additional exponential pole strength decay term within summation—due to integration over limited film thickness *t*—can be neglected here.
[34] M. J. Donahue, D. G. Porter, *OOMMF User's Guide, Version 1.0: Interagency Report*, National Institute of Standards and Technology, Gaithersburg, MD **1999**.
[35] W. Wang, C. Mu, B. Zhang, Q. Liu, J. Wang, D. Xue, *Comp. Mater. Sci.* **2010**, *49*, 84–87.
[36] Asylum Research, 6310 Hollister Ave, Santa Barbara, CA 93117.
[37] R. Engel-Herbert, D. M. Schaadt, T. Hesjedal, *J. Appl. Phys.* **2006**, *99*, 113905.